Safe-by-Design Iron Oxide Nanofertilizers: Ecotoxicological Screening and Concentration-Dependent Physiological Responses in Zea mays L

Simone Y. Fernandes

simoneyasuda@hotmail.com

Universidade Estadual de Mato Grosso do Sul

Montcharles S. Pontes

Universidade Federal de Mato Grosso do Sul

Jaqueline S. Santos

Universidade de São Paulo

Renato Grillo

Universidade Estadual Paulista (Unesp)

Gilberto J. Arruda

Universidade Estadual de Mato Grosso do Sul

Etenaldo F. Santiago

Universidade Estadual de Mato Grosso do Sul

Research Article

Keywords: Engineered nanomaterials, Oxidative stress, Chlorophyll a fluorescence, Environmental safety, Hormesis, Safe-by-design

Posted Date: July 6th, 2026

DOI: https://doi.org/10.21203/rs.3.rs-10082073/v1

Additional Declarations: No competing interests reported.

Abstract

The development of engineered nano formulations is a pivotal strategy to improve the bioavailability of poorly mobile micronutrients like iron (Fe), minimizing agrochemical runoff and environmental footprint. However, establishing clear ecotoxicological thresholds for these novel materials remains crucial for safe agricultural application. Here, we report the synthesis, comprehensive physicochemical characterization, and cellular toxicity screening of chitosan-coated iron oxide nanoparticles (CS:Fe_3O_4 NPs). The synthesized composite was structurally and thermally characterized using Fourier-transform infrared spectroscopy (FTIR), scanning electron microscopy coupled with energy-dispersive X-ray spectroscopy (SEM/EDX), and differential thermal analysis (DTA/DSC). FTIR confirmed the successful formation of the composite via characteristic N-H and Fe–O stretching vibrations, while SEM/EDX revealed spherical morphology (average diameter of 114 nm) consisting of Fe, C, and O. The physiological, biochemical, and toxicological effects were evaluated in *Zea mays* L. leaf discs exposed to a concentration range of 0 (0), 1 (10), 20 (200), 40 (400), 60 (600), 80 (800) and 100 (1000) μg mg^{-1} (μg L^{-1}). Moderate application doses induced a hormetic effect, significantly enhancing photosynthetic pigment biosynthesis and electron transport efficiency in photosystem II (PSII). Conversely, high concentrations triggered severe oxidative stress, characterized by significant accumulations of hydrogen peroxide (H_2O_2) and malondialdehyde (MDA), indicating lipid peroxidation of cellular membranes. This toxicity resulted in a severe depletion of non-enzymatic defense compounds including total phenolics, flavonoids, and tannins accompanied by a reduction in guaiacol peroxidase (GPOX) and ascorbate peroxidase (APX) activities. To cope with excess iron, the plant activated a catalase (CAT) mediated antioxidant defense pathway. In conclusion, CS:Fe_3O_4 NPs induce concentration-dependent modulations in PSII functionality and plant metabolism. These findings successfully establish a safe environmental and agronomic application ceiling (< 60 (600) μg mg^{-1} (μg L^{-1})), providing critical baseline parameters for the sustainable management of iron nanofertilizers in precision agriculture.

Introduction

Global population estimates project approximately 9 billion people by 2050, highlighting the urgent need for substantially increased food production (Pereira et al., 2021; Pontes et al., 2025; Santos et al., 2025). To address this demand, the adoption of advanced technologies is increasingly necessary to achieve agriculture that is more efficient, productive, and environmentally sound, particularly given the concurrent challenges of climate change and intense pressure on natural resources (FAO, 2024). However, the drive for increased agricultural output inherently escalates the reliance on synthetic inputs, particularly agrochemical fertilizers. Conventional fertilizer application faces critical limitations concerning durability (field persistence), cost-effectiveness, and environmental impact, leading to poor nutrient use efficiency, high rates of nutrient loss, limited bioavailability, and adverse effects on non-target organisms (Larsen et al., 2021). In response, nanotechnology has emerged as a promising disruptive alternative with lower environmental risk and greater biological effect (Zhang and Goss, 2022), capable of enhancing crop productivity (Haris et al., 2023). Despite this substantial promise, nano-enabled agriculture presents

several significant knowledge gaps, particularly regarding the dose-dependent mechanisms of nano-impact on plant physiology and stress responses.

Fertilizers are indispensable inputs in modern agriculture, directly correlating with food yield by supplying essential nutrients required for optimal plant growth (Penuelas et al., 2023). However, nutrients can be a critical limiting factor due to deficiency or excess in the soil, making it crucial that they exist in a form that can be assimilated by the plant (Morgan and Connolly, 2013). This challenge is particularly acute for low-mobility micronutrients like Iron (Fe), which are prone to soil fixation. Iron is essential for photosynthesis, cellular respiration, and the formation of enzymes and proteins (Kobayashi et al., 2019), and its deficiency can damage the photosynthetic apparatus and chlorophyll synthesis, leading to necrosis and leaf chlorosis (Li et al., 2021). The availability of iron is limited primarily by the low solubility of the ferric form (Fe^{3+}) in aerobic soils, while the ferrous form (Fe^{2+}) is assimilated more readily through ferric chelate reductase enzymes (Zuluaga et al., 2023). Consequently, synthetic chelated iron such as EDTA, EDTPA, and EDDHA is commonly applied to promote plant absorption (Madhupriya et al., 2024).

Alternatively, supplying iron via microparticles is an intelligent way to make this element available and absorbable to plants (Razzaq and Zhou, 2025). Fe_3O_4 microparticles can be obtained through various methods, including the use of plants and chemical agents as reducing agents and precipitants (Nguyen et al., 2021), and their magnetic properties are widely exploited in targeted delivery and controlled release (Pontes et al., 2024). After overcoming biological barriers and internalization, metallic NPs undergo oxidation and release ions for plant metabolism (Anuta et al., 2025). Polymer-chelated iron oxide systems, such as Fe_3O_4 chelated with N-ethylenediamine and N-bis(2-hydroxyphenylacetic acid), exhibit greater enzymatic activity and lower ROS production in *Zea mays* (Jalali et al., 2016). Conversely, evaluations by Lau et al. (2020) with Fe_3O_4 coated with NH_3 amine groups showed no effects on leaf and root growth in *Solanum lycopersicum*. To enhance safety, chitosan (CS) a polymer with hydroxyl (– OH) and amino (–NH_2) groups serves as a stabilizing matrix that prevents nanoparticle aggregation, acts as an elicitor of plant defenses, and enhances the bioactivity of the iron core (Sahin et al., 2022).

Corn (*Zea mays* L.) cultivation is the third largest food source, with an extensive world production where Brazil, the United States, and Argentina stand out as major producers (FAO, 2024; USDA, 2025). Its caryopses contain essential macro- and micronutrients, including potassium and iron (Baranowska et al., 2023). In this species, iron is a fundamental cofactor for proteins essential to photosynthetic activity, acting directly on electron transport structures, and engineered nanoparticles have shown great potential to modulate these photosynthetic electron pathways and enzyme activities (Li et al., 2024). However, the strategic development of nanoformulations must prioritize detailed assessments of their modes of action and physiological effects while paying critical attention to potential impacts on non-target organisms (Pontes et al., 2023). Our study directly addresses this necessity by synthesizing and characterizing iron nanoformulations chelated with chitosan (CS:Fe_3O_4 NPs) and critically evaluating their dose-dependent effects on *Zea mays* L., focusing on photosynthetic activity, chlorophyll content, antioxidant enzymatic activity, and membrane damage to establish robust parameters for safe and sustainable precision agriculture.

Materials and methods

2.1. Chemical materials

2.2. Synthesis of Fe $_3$ O $_4$ iron oxide nanoparticles

Iron oxide nanoparticles were prepared by the chemical coprecipitation method, according to the stoichiometry of Eq. 1. Chloride salts were used as precursors; 20 mL of $FeCl_2$ $4H_2O$ (0.025 mol L^{-1}) and 20 mL of $FeCl_3$ $6H_2O$ (0.050 mol L^{-1}) were dissolved in 50 mL of distilled water. The solution was then heated to 70°C and nitrogen was purged to remove oxygen during the dripping of 50 mL of sodium hydroxide solution (NaOH 2M). The color change from brown to black indicated the formation of iron oxide. The solution was kept under magnetic stirring for 8 hours at a speed of 300 rpm. Subsequently, the solution particles were attracted with a neodymium magnet and washed with ethanol (99%) and distilled water in triplicate to remove organic matter according to Grillo et al. (2016). Finally, they were transferred to Petri dishes and the solution was evaporated at room temperature to obtain the solid NPs.

$$\mathrm{Fe^{2+}\,(aq) + 2Fe^{3+}\,(aq) + 8OH^{-}\,(aq) \rightarrow\ Fe_3O_4\,(s) + 4H_2O}$$ Eq. (1)

2.3. Chitosan solution preparation

A 0.5 g L^{-1} chitosan solution (Sigma Aldrich 99%) was prepared in 100 mL of 0.4 M acetic acid, maintained on magnetic stirring (300 rpm) for 1 hour at room temperature (± 25 ºC) (Bavel et al., 2023).

2.4. Fe_3O_4 with chitosan (CS)

50 mg of Fe_3O_4 (solid) were slowly added to a solution of CS NPs (0.5 g L^{-1}) under stirring, and the mixture was kept under stirring for 24 hours. Subsequently, the Fe_3O_4 NPs were stirred at high speed of 3.000 rpm/min for 10 minutes, followed by filtration through a 2 µm membrane using a vacuum pump. Figure 1 shows the CS groups that chelate Fe_3O_4 ions. The working solution with a final concentration of 0.5 g L^{-1} was kept refrigerated at 4°C.

2.5. Physicochemical characterization of nanomaterials

2.5.1. Fourier-transform infrared spectroscopy (FTIR)

Fourier transform infrared (FTIR) spectroscopy was performed using a Thermo Nicolet Nexus 670 spectrophotometer with KBr pellets in the spectral range of 4000–400 cm^{-1}. The spectrophotometer was purged with dry air to remove any water vapor. All spectra were obtained at 4 cm^{-1}. All spectra were obtained with a resolution of 8 cm and 128 scans, and a carbon black spectrum was collected as a reference. All data were collected in triplicate and at room temperature.

2.5.2. Scanning Electron Microscopy (SEM) with Energy-Dispersive X-ray Spectroscopy (EDS)

Morphological characterization used a ZEISS Sigma 360 VP field-emission SEM with secondary electron detector. Samples were dispersed onto carbon tape on aluminum stubs and sputter-coated with gold for 90 s to ensure conductivity and minimize charging. Images were acquired at 2.0–10.0 kV accelerating voltage, 4.2–9.8 mm working distance, and 3,200 – 100,000 x magnification to capture hierarchical architecture and surface details. Semi-quantitative elemental analysis was performed using used an Oxford Instruments EDS detector integrated with the ZEISS Sigma 360 VP SEM at 20 kV. Elemental composition represents averaged measurements from five randomly selected regions. Due to hierarchical porous microstructure inducing irregular electron scattering and variable X-ray take-off angles, quantification should be considered semi-quantitative with typical uncertainties of ± 2–5 at%.

2.6. Differential Thermal Analysis (DTA) and Differential Calorimetry (DSC)

DTA/DSC curves were obtained by thermal analysis. Samples were analyzed in synthetic air and nitrogen atmospheres. In both analyses, heating from 20 to 900°C was used, with an N2 air flow and a heating rate of 10°C per min^{-1} in an alumina crucible.

2.7. Plant material

Planting was carried out in the experimental area of the Campus of the State University of Mato Grosso do Sul, Brazil (Latitude 22°13'18.54" S and Longitude 54°48'23.09" W). Before planting, NPK (proportions of 20-10-10, in the form of NH_4NO_3, $NH_4H_2PO_4$ and K_2SO_4, respectively). Commercial seeds of the CG1058 cultivar of *Zea mays* L. were used for planting, for this purpose, two seeds were placed 5 cm deep in each 30 cm planting hole.

2.7.1. Bioassay with leaf discs containing CS and CS:Fe_3O_4 NPs

The leaf disc method was used to evaluate the effects of NPs on biochemical and photosynthetic parameters (Pontes et al., 2021). Healthy leaves from the vegetative stage (V10) of *Zea mays* plants were collected to obtain leaf discs. Discs with a diameter of 12.33 mm were cut in the leaf blade region along the entire length of the leaves, except for the middle. The leaf disc treatments were standardized by the ratio of µg of CS and CS:Fe_3O_4 NPs at an initial concentration of 0.5 g L^{-1} per gram of leaf discs (500 mg). For this, solutions at concentrations of 1, 20, 40, 60, 80, and 100 µg mg^{-1} were prepared in buffer solutions of monobasic potassium phosphate (KH_2PO_4) and dibasic potassium phosphate (K_2HPO_4) at pH 7. Two controls were used, with the control treatment being potassium phosphate buffer without Fe_3O_4 and a control with CS solution (0.5 g L^{-1}). Then, the leaf discs were placed in the treatments, with five repetitions at room temperature (± 25 ºC) and light (Fig. 2).

2.7.2. Chemical parameters of solutions with CS and CS:Fe_3O_4 NPs with Zea mays leaf discs

The parameters pH, electrical conductivity (μS cm^{-1}), total dissolved solids (ppm), and redox potential (mV) were measured using a multiparameter probe. Measurements of the solutions were taken before the leaf discs were applied, and after 24 hours of exposure, the discs were removed and the measurements were taken again.

2.7.3. Chlorophyll fluorescence induction (ChlF)

The ChlF was determined at room temperature (25 ± 1°C) using a Handy PEA portable fluorometer (Hansadech Instruments Ltd., Pentney, UK). Leaf discs (15 units) were clipped and kept in the dark for 30 minutes. After dark adaptation, a single pulse of red light at 650 nm and a saturation intensity of 3500 μmol m^{-2} s^{-1} was fired to excite chlorophyll. The following parameters were obtained according to the transient intersections: (O-step) F0, fluorescence intensity at 50 μs; Fk, fluorescence intensity at 300 μs; (J-step) Fj, fluorescence intensity at 2 ms; (I-step) FI, fluorescence intensity at 30 ms; (P-step) Fm, maximum fluorescence. The following parameters were obtained: initial fluorescence (F0); maximum fluorescence (Fm); maximum quantum efficiency potential of PSII (Fv/Fm); specific energy fluxes per reaction center for: absorption (ABS/RC); dissipation (Dio/RC); electron transport (ETo/RC); energy capture (TRo/RC); and energy-absorbed performance index (PI_{ABS}). Total photosynthetic index (PI_{TOTAL}). The data obtained were used to calculate photochemical and biophysical parameters according to Strasser et al. (2004).

2.7.4. Photosynthetic pigment content

The content of chlorophyll *a*, chlorophyll *b*, and total chlorophyll, and carotenoids were determined in leaf discs. For this, 100 mg of fresh mass was macerated in 5 mL of 96% (v/v) ethanol:water, then kept in the dark for 24 hours. The material was then centrifuged at 12.000 rpm for 30 minutes at 4°C. The supernatant was measured using a spectrophotometer (UV-5200 Global Trade Technology). Absorbance was evaluated and calculated according to the equations of Lichtenthaler and Wellburn (1983). Pigment concentrations were expressed in μg mg^{-1} of fresh mass (FW).

[Chlorophyll *a*] = (13.95 × *Abs*665) − (6.88 × *Abs*649)	**Equation (2)**
[Chlorophyll *b*] = (24.96 × *Abs*649) − (7.32 × *Abs*665)	Equation (3)
[Total chlorophyll] = Chl*a* + Chl*b*	Equation (4)
[Total carotenoids] = [(1000 × *Abs*470) − (2.05 × Chl*a*) − (114.8 × Chl*b*)] / 245	Equation (5)

2.7.5. Quantification of total flavonoid, phenolic, and tannin content

For the analysis of flavonoid, phenolic, and tannin content, the methodologies of Lin and Tang (2007), Bonoli et al. (2004), and Pansera et al. (2003), respectively, were followed. 100 mg of fresh mass were macerated in 5 mL of 95% (v/v) ethanol:water, followed by centrifugation at 4000 rpm for 30 minutes. For flavonoids, 500 µL of the extract, 100 µL of 10% aluminum chloride hexahydrate ($AlCl_3$), 100 µL of 1 M potassium acetate (CH_3COOK), 1.5 µL of 95% alcohol, and 800 µL of distilled water were homogenized. Absorbance was measured at 415 nm using a spectrophotometer. An analytical curve was constructed to calculate flavonoid concentrations, using quercetin as an analytical standard (Sigma-Aldrich) and expressed in µg mg^{-1} of FW. For phenolics, 500 µL of the extract was homogenized with 1.5 µL of 2% sodium carbonate, 500 µL of Folin-Ciocalteu (1:10 v/v) and 500 µL of distilled water and left to stand for 30 minutes. Absorbance was measured at 760 nm using a spectrophotometer. An analytical curve was constructed to calculate phenolic concentrations, using gallic acid as an analytical standard (Sigma-Aldrich), and expressed in µg mg^{-1} of FW. For tannins, 500 µL of the extract was homogenized in 500 µL Folin-Ciocalteu (0.05%), 1.5 mL of 0.5 M sodium carbonate (Na_2CO_3), and 500 µL of distilled water. Absorbance was measured at 730 nm using a spectrophotometer (UV-5200, Global Trade Technologic). An analytical curve was constructed to calculate tannin concentrations, using an analytical standard of tannic acid (Sigma-Aldrich) and expressed in µg mg^{-1} of FW.

2.7.6. Enzymatic activity

To evaluate enzymatic activity, 100 mg of fresh mass were placed in a crucible (containing liquid nitrogen) and macerated with 2 mL of refrigerated extraction solution (100 mM potassium phosphate buffer pH 7.5, 1 mM dithiothreitol, 4% polyvinylpyrrolidone). After homogenization, the samples were centrifuged at 10.000 rpm for 30 minutes at 4°C. The supernatant was used for assays of the enzymes superoxide dismutase (SOD), catalase (CAT), guaiacol peroxidase (GPOX), and ascorbate peroxidase (APX), according to the methodology of Giannopolitis and Ries (1977), Kraus et al. (1995), Matsuno and Uritani (1972), and Moldes et al. (2008), respectively. For a 50 µL SOD sample, 2.5 mL of reaction solution (3.0 mL of 0.1 M potassium phosphate buffer; 2.0 mL of L-methionine; 2.0 mL of 0.44 mM nitrotetrazolium; 2.0 mL of 100 mM ethylenediaminetetraacetic acid; 0.8 mL of 1 mM riboflavin) were homogenized and kept for 15 minutes under light (20 W) at 25°C. As a control, samples without the addition of the extract were used under dark conditions. Absorbance was measured at 560 nm using a spectrophotometer. The difference in ABS between the samples kept in light and dark conditions was calculated and used to determine the SOD activity. The result was expressed in SOD units (U) per mg^{-1} of FW. For CAT, 50 µL of the sample was added to 925 µL of 100 mM potassium phosphate buffer pH 7.50 and 25 µL of 10% H_2O_2; absorbance reading was taken at 240 nm. For APX, 50 µL of the sample was homogenized with 800 µL of 80 mM potassium phosphate buffer pH 7.00, 25 µL of 5 mM ascorbic acid, 100 µL of 1 mM ethylenediaminetetraacetic acid (EDTA), and 25 µL of 1 mM H_2O_2; absorbance readings were taken over 1 minute at 290 nm. GPOX: 10 µL of the sample was added to a solution containing phosphate citrate buffer (0.2 M dibasic sodium phosphate and 0.1 M citric acid pH 5.00) and 0.2% guaiacol and homogenized in a vortex mixer. To this solution, 50 µL of 9.8 mM H_2O_2 was added and stirred, followed by heating for 15 minutes at 30°C. Finally, the samples were placed in an ice bath and 50 µL of 2% sodium

metabisulfite was added, and the absorbance was measured at 450 nm. The results were expressed in nmol min^{-1} mg^{-1} of FW.

2.7.7. Hydrogen peroxide (H_2O_2) and lipid peroxidation content (MDA)

To determine H_2O_2 and MDA content, 100 mg of fresh mass was macerated in 2 mL of 0.1% trichloroacetic acid (TCA) and 20% PVPP, then centrifuged at 13.000 rpm for 10 minutes at 4°C. For H_2O_2 (Alexieva et al., 2001), 200 µL of the supernatant was homogenized in 200 µL of 100 mM potassium phosphate buffer 7.50 and 800 µL of 1M KI (potassium iodide) and kept in the dark for 30 min, then the absorbance was read at 390 nm. Lipid peroxidation was measured as malondialdehyde (MDA) content. 250 µL of the supernatant was homogenized in 1 mL of 20% TCA containing 0.1% thiobarbituric acid. The samples were heated to 95°C for 30 min, then cooled in an ice bath. After reaching room temperature, absorbance readings were taken at 532 nm and 600 nm. The MDA content was calculated using the following equation and expressed in nmol mg^{-1} of FW.

[MDA nmol/mg] = Abs (532–600) / ε155	**Eq. (6)**
ε155 mM^{-1} cm^{-1} = molar extinction coefficient	

3. Data analysis

The data were subjected to the normality test (Shapiro-Wilk) to assess the distribution of treatment means. Parametric data were analyzed by two-way ANOVA followed by post hoc tests, whereas non-parametric comparisons were assessed using Kruskal–Wallis with Dunn's test. The BioEstat 5.3 software with a significance level of $p < 0.05$ was used in all statistical analyses.

Results and discussion

4.1. Characterization

The FTIR spectra of Fe_3O_4 NPs, CS, and CS:Fe_3O_4 NPs are shown in Fig. 3A. The formation of the CS:Fe_3O_4 NPs nanocomposite is supported by changes in the amide-related absorption bands. The band at 568 cm^{-1} corresponds to the Fe – O vibration of magnetite, confirming the presence of Fe_3O_4 (Ansari et al., 2018). In the CS, characteristic bands at 2870 cm^{-1} (– CH_2), 1640 cm^{-1} (C = O), 1551 cm^{-1} (– NH_2), and 1060 cm^{-1} (C – O) indicate the amide and polysaccharide groups of chitosan (Lustriane et al., 2018). The shift and stretching of the amide bands in the composite further suggest the formation of a chitosan–magnetite complex (Appu et al., 2021).

The elemental composition of Fe_3O_4 NPs is presented in the spectra containing the mass data (%) (Fig. 3B), with Fe 40% and O 60%; the identified elements indicate an absence of impurities. For chitosan,

C 58%, N 8% and O 33% were identified, elements that form chemical groups such as NH_2 in the chemical structure. In CS:Fe_3O_4 NPs, the spectra show C, 58%, N 7%, O 34% and Fe 0.11%, indicating the presence of chemical groups originating from Fe_3O_4 and chitosan.

Micrographic images of CS, Fe_3O_4 NPs, and CS:Fe_3O_4 NPs are shown in Figs. 3C-E. Chitosan has a lamellar structure with an irregular surface and cavities, which can favor adsorption and interaction processes. The Fe_3O_4 NPs have a predominantly spherical shape and homogeneous distribution; the particle size has an average diameter of 114 ± 9 nm. In the nanostructure formed by CS and Fe_3O_4 NPs, the adhesion and distribution of the Fe_3O_4 NPs along the surface of the CS is observed, maintaining the spherical morphology and average particle diameter of 114 ± 15 nm (Fig. 3E). The CS composed of amines (– NH_2) and Fe_3O_4 NPs with abundant hydroxyl groups (Fig. 3A) forms a hybrid system, in which bonds occur between the aforementioned chemical groups (Silveira et al., 2021). Chitosan solubilized in an acidic medium undergoes protonation ($–NH_2 \rightarrow –NH_3^+$) and is used to adsorb anionic ions, with extensive results for the adsorption of metal oxides (Guibal et al., 2004; Wujcicki et al., 2026).

4.2. Thermal characterization

The thermograms are presented by DTA and DSC obtained in the range of 20–900 ºC (Fig. 4). The oxidation-reduction peaks were recorded in DSC thermograms, along with the mass loss events (%) / DTA of the samples. The DTA thermogram shows residual mass of 78%, 21%, and 24% for Fe_3O_4 NPs, CS, and CS:Fe_3O_4 NPs, respectively. Our results show a mass loss in the range of 22–270 ºC, suggesting water removal. For Fe_3O_4 NPs, two events were observed in the ranges of 100–270 ºC and 270–370 ºC, each with a 4% loss.

Magnetite exposed to high temperatures undergoes oxidation-reduction reactions, which modify its chemical structure. At temperatures above 500°C, the oxidation reaction of Fe_3O_4 is recorded by the exothermic peak in the range of 700–760°C, obtained by the DSC thermogram (Fig. 4A). Results from Sanders and Gallagher (2006), corroborate the exothermic events in magnetite samples. This event, resulting from the oxidation reaction, indicates the conversion of Fe^{2+} to Fe^{3+} in the formation of Fe_3O_4, with Fe_2O_3 gradually forming at temperatures above 700 ºC (Fumis et al., 2022).

Figure 4B shows the DTA/DSC thermograms of CS. A mass loss of 48% occurred in the range of 270–370°C, followed by 21% in the range of 370–900°C. The two sharp peaks of chitosan mass reduction indicate manipulation reactions of the amide and acetyl chains (Villar et al. 2018). Results from Nam et al. (2010), suggest that the gradual loss of chitosan mass above 340°C is due to the degradation reaction of 2-amino-2-deoxy-D-glucopyranose (GlcN) units. Figure 4C shows the DTA/DSC thermogram of CS:Fe_3O_4 NPs. The thermal behavior between CS and CS:Fe_3O_4 NPs is similar, differing only in temperature range and residual mass.

DTA results show the first event at 25–100 ºC, with a loss of 14%. The greatest mass loss of 34% occurred in the range of 250–370 ºC. The DSC thermogram of CS:Fe_3O_4 NPs begins with an endothermic peak in the range of 25–120°C, an exothermic peak between 246–300°C with a slight shift compared to pure CS, and a peak of lower intensity. Another endothermic peak is observed in the 430–630°C range, followed by a continuous increase up to 900°C. The nanocomposite curve profile shows changes in intensity and shift, with characteristics similar to those of the thermograms of CS and pure Fe_3O_4, indicating an interaction and functionalization of the compounds (Ates et al., 2018). The residual mass of CS:Fe_3O_4 NPs compared to CS may suggest the formation of the polymer-metal complex. The chitosan matrix in metals is an excellent carrier of actives, including metals, corroborating the results of Pereira et al. (2017), in which chitosan chelation with metals (Cu, Zn and Ni) yields residues of greater mass than CS alone.

4.3. Chemical parameters of solutions with CS and CS:Fe_3O_4 NPs on Zea mays leaf discs

Figure 5 presents the data for pH, electrical conductivity, total dissolved solids, and redox potential obtained from solutions where *Zea mays* leaf discs were exposed to CS and CS:Fe_3O_4 NPs. The results show that, except for pH, concentration was the most relevant factor, and little difference in values was observed over time. The pH values after exposure showed a reduction for both CT and CS treatments, whereas leaves treated with CS:Fe_3O_4 NPs, showed no significant reduction (Fig. 5A). Results for electrical conductivity and total dissolved solids (Figs. 5B-C) show a similar profile, with increased values when the CS:Fe_3O_4 NPs concentrations were increased. The grate values for total dissolved solids after exposure (Figure C), observed at concentrations of 60, 80, and 100 µg mg^{-1}, may be related to the release of leaf exudates through interaction with the NPs. Treatments with CS:Fe_3O_4 NPs had a higher oxidizing potential than the control and CS before exposure to leaf discs (Fig. 5D), suggesting that Fe_3O_4 compounds are oxidized. Increases in redox potential values were also observed in the control, after 24 hours, suggesting that compounds are oxidized in the absence of CS or NPs presence. The chemical parameters evaluated were clearly modulated by the NPs, given that metallic nanoparticles are suggested to act as conductive pathways within the vascular system. Uptake and distribution can occur without repulsion; however, depending on the amount of material involved, this may lead to increased exudate release from the biological system—as evidenced by higher values for electrical conductivity and redox processes affecting the system's pH (Merino-Treviño et al., 2024).

4.4. Effect of CS and CS:Fe_3O_4 NPs on ChlF and photosynthetic pigment content

Chlorophyll *a* fluorescence induction kinetics were observed in *Zea mays* leaf discs under different nanoparticle treatments (Fig. 6) to assess their effects on the structure and function of the photosynthetic apparatus. In general, treatments with particles reduced the intensity of ChlF emission, especially at higher CS:Fe_3O_4 concentrations, with the CS treatment being the closest to the control.

Regarding the fluorescence steps, the sigmoid pattern of the curves was maintained across all treatments. The main changes in intensity began to appear in the O-J interval at 1 μg mg^{-1} of CS:Fe_3O_4, with the maximum fluorescence (Fm) suppressed at the highest dose (100 μg mg^{-1}). For samples treated with CS, or with CS:Fe_3O_4 at concentrations > 20 μg mg^{-1}, reductions in ChlF *a* intensity are observed from the I-P phase suggesting alterations in the PQ-pool. The ChlF behavior is dose-dependent, and the steps affected by the treatments indicate a change in electron transfer from quinone A (QA) to quinone B (QB) in photosystem II (J-I). Analysis of the OJIP (Kautsky) curve provided parameters describing PSII behavior. F0 (step O) showed increased photon capture at the reaction center in PSII at 20, 40, and 80 μg mg^{-1}, followed by a decrease at 100 μg mg^{-1}. For Fm (step P), the concentration of 1 μg mg^{-1} led to the highest maximum fluorescence index, indicating that low concentrations of Fe_3O_4 suggest that the electron transfer capacity to QB is temporarily limited or saturated. The maximum quantum efficiency of PSII (Fv/Fm) from a concentration of 40 μg mg^{-1} shows lower values, but does not differ significantly ($p < 0.05$) from CT, although the values are within the normal range for maximum efficiency, except at 100 μg mg^{-1} of CS:Fe_3O_4 (0.6), which indicates damage to PSII.

The PSII reaction center results were obtained using absorption, dissipation, capture, and transport parameters (Table 1). Absorption (ABS/RC) and dissipation (DI0/RC) parameters were higher with the iron oxide treatment, with DI0/RC showing a significant difference ($p < 0.05$) compared to the control. Electron Transport (ET0/RC) and capture (TR0/RC) per reaction center did not show a significant difference ($p < 0.05$); however, the 60 μg mg^{-1} concentration showed the highest value. Although the results not show a significant gain, they indicate the effective electron transport in the PSII. The PI_{ABS} photosynthetic performance index decreased with increasing CS:Fe_3O_4 concentration, whereas PI_{TOTAL} showed the highest photosynthetic efficiency (PSI-PSII) at 20 μg mg^{-1} of CS:Fe_3O_4.

Iron-based materials in plants can make electrons available, which consequently act on the photosynthetic apparatus through electron transition and chlorophyll biosynthesis (Schmidt et al., 2020). This hypothesis corroborates the results obtained by Li et al. (2020), which show that the interaction of Fe_3O_4 NPs with isolated chloroplasts from *Zea mays* L. acts as a supplier of electrons to be captured and transported in the PSII to PSI apparatus, consequently increasing photosynthetic efficiency. Gamito et al. (2024), for *Triticum aestivum* L. exposed to Fe_3O_4 NPs, Fm was higher with the highest concentration, while the maximum quantum efficiency was lower at the highest concentration (150 mg L^{-1}). This means that the concentration factor significantly influences the mode of action of NPs in photosynthesis.

Table 1
Effect of CS NPs and CS:Fe_3O_4 NPs on initial fluorescence (F0). Maximum fluorescence (Fm). Maximum quantum efficiency of the donor side of PSII (Fv/F0). Maximum quantum efficiency of photosystem II (Fv/Fm). On specific energy fluxes per reaction center for: Absorption (ABS/RC). Dissipation (DI0/RC). Electron transport (ETo/RC). Energy capture (TRo/RC). Energy-absorbed performance index (PI_{ABS}). Total photosynthetic index (PI_{TOTAL}). In *Zea mays* leaf discs exposed for 24 hours.

µg mg^{-1}	F_0	Fm	Fv/F_0	Fv/Fm	*Abs*/RC	Di_0/RC	ET_0/RC	TR_0/RC	PI_{ABS}	PI_{TOTAL}
CT	627 ± 6[b]	3025 ± 7[b]	4.10 ± 0.21[a]	0.80 ± 0.01[a]	2.32 ± 0.21[a]	0.49 ± 0.05[b]	1.00 ± 0.05[a]	1.88 ± 0.11[a]	2.63 ± 0.22[a]	1.02 ± 0.32[bc]
CS	612 ± 9[c]	2891 ± 7[c]	3.75 ± 0.41[a]	0.80 ± 0.02[a]	2.50 ± 0.31[a]	0.55 ± 0.05[ab]	1.00 ± 0.06[a]	1.97 ± 0.05[a]	1.61 ± 0.41[b]	1.13 ± 0.41[bc]
1	628 ± 9[b]	3265 ± 9[a]	4.01 ± 0.32[a]	0.80 ± 0.02[a]	2.30 ± 0.21[a]	0.47 ± 0.05[b]	1.02 ± 0.08[a]	1.77 ± 0.06[b]	2.22 ± 0.31[a]	1.34 ± 0.22[b]
20	648 ± 9[a]	2760 ± 9[c]	3.51 ± 0.41[a]	0.76 ± 0.05[a]	2.51 ± 0.21[a]	0.57 ± 0.05[ab]	1.06 ± 0.08[a]	1.94 ± 0.10[a]	1.65 ± 0.51[b]	1.53 ± 0.42[b]
40	621 ± 6[b]	2670 ± 7[c]	3.16 ± 0.42[a]	0.74 ± 0.02[a]	2.60 ± 0.21[a]	0.61 ± 0.04[a]	1.01 ± 0.08[a]	1.86 ± 0.10[a]	1.41 ± 0.22[b]	0.82 ± 0.11[c]
60	634 ± 4[a]	2540 ± 8[d]	3.45 ± 0.31[a]	0.75 ± 0.02[a]	2.61 ± 0.11[a]	0.60 ± 0.05[a]	1.07 ± 0.05[a]	2.00 ± 0.09[a]	1.52 ± 0.16[b]	1.43 ± 0.31[b]
80	640 ± 4[a]	2570 ± 9[d]	2.14 ± 0.52[b]	0.72 ± 0.05[a]	2.61 ± 0.22[a]	0.60 ± 0.05[a]	0.98 ± 0.06[a]	1.97 ± 0.07[a]	0.71 ± 0.22[c]	0.82 ± 0.12[c]
100	580 ± 7[d]	2346 ± 6[e]	2.18 ± 0.61[b]	0.70 ± 0.05[a]	2.60 ± 0.11[a]	0.65 ± 0.05[a]	1.00 ± 0.09[a]	1.98 ± 0.10[a]	0.92 ± 0.22[c]	0.82 ± 0.12[c]

The results are represented by the means followed by the standard deviation (±). In the same column, different letters indicate a significant difference between treatments, according to the two-way ANOVA test (t-test).

Figure 7 shows the photosynthetic pigments. A significant increase in pigment content compared to CT occurred in all treatments. The concentration of 20 µg mg^{-1} showed the highest content of Chl-*a*, total Chl, and carotenoids (Fig. 7A, C, D). The highest content of Chl-*b* was at the concentration of 40 µg mg^{-1} (Fig. 7B). The increase in carotenoid content is significant because these molecules protect PSII from photoinhibition by accepting electrons and leading the PSII complex to a lower energy state (Apel and Hirt

2004). CS:Fe_3O_4 NPs can affect energy absorption and the glutamate pathway, a precursor of Chl-*a* (Li et al., 2020). It is suggested that Fe-based NPs increase Chl-*a* content by making Fe ions available for the photosynthetic process. The increase in pigment content has been observed in other plant species, such as *Zea mays*, *Triticum aestivum*, *Cannabis sativa* L., *Hordeum vulgare* (Yan et al., 2020, Feng et al., 2022, Deng et al., 2022, Tombuloglu et al., 2024).

4.5. Effect on enzyme activity (SOD, CAT, APX, GPOX)

Our results show that treatments with CS and CS:Fe_3O_4NPs affected enzymatic activity, depending on the concentration (Fig. 8). SOD enzyme activity was reduced with CS, while CS:Fe_3O_4 NPs showed a slight reduction ($p < 0.05$) (Fig. 9A). CAT enzyme activity increased at concentrations of 40 to 100 µg mg^{-1} (Fig. 8B).

The highest APX activity was observed at a dose of 40 µg mg^{-1} (Fig. 8C), while GPOX enzyme activity increased significantly at 40 µg mg^{-1}, being reduced at higher doses (Fig. 8D). Enzymatic activity corresponds to the first line of antioxidant defense. Therefore, the effects of reduction or gain represent the plant's defense and/or yield. Our results show a significant change in enzymatic activity at higher NP concentrations, corroborating the increase in H_2O_2 and MDA content (Fig. 10). It is suggested that higher doses of CS:Fe_3O_4 NPs may cause damage to cell membranes (Fig. 10). Our results show an increase in CAT activity at concentrations of 40 to 100 µg mg^{-1}, an enzyme responsible for H_2O_2 oxidation; however, H_2O_2 levels are higher than CAT levels, which may have caused a reduction in APX and GPOX activity (Wang et al., 2019). Fe nanoformulations, exhibit size, permeability, and availability characteristics that enhance metabolic activity for maize and other crops (Elanchezhian et al., 2017; Haydar et al., 2022).

4.6. Effect on flavonoid, phenolic and tannin content

Total flavonoid content increased at a concentration of 20 µg mg^{-1}, while concentrations of 80 and 100 µg mg^{-1} showed lower content compared to the control. Total phenolic content increased at concentrations of 1 and 20 µg mg^{-1}, but contractions from 40 to 100 µg mg^{-1} were smaller compared to the control. Total tannin compounds showed a significant increase from 1 to 80 µg mg^{-1}, but decreased at 100 µg mg^{-1} (Fig. 9). Non-enzymatic antioxidant defense acts in the chelation of metal ions, preventing the generation of reactive oxygen species (Ahmed et al., 2022, Kejík et al., 2022), suggesting that hydroxyl and carbonyl groups are involved in this process. The reduction in the amount of these compounds at higher concentrations of CS:Fe_3O_4 NPs may be associated with increased lipid peroxidation and H_2O_2 (Fig. 10A, B), being inefficient in oxidizing free radicals. Results from Kalisz et al. (2021) suggest that Fe_2O_3 NPs stimulate the antioxidant capacity of lettuce by increasing the content of phenolics and flavonoids.

4.7. MDA and hydrogen peroxide content - H_2O_2

Hydrogen peroxide (H_2O_2) and MDA levels increased with concentrations of 40, 60, 80, and 100 µg mg^{-1} (Fig. 10). The results show that high concentrations of CS:Fe_3O_4 NPs can induce oxidative stress; the Fe oxide form can be converted into Fe ions and trigger oxidative reactions in plant tissue (Muller et al., 2015). Fe ions can react with H_2O_2 and generate hydroxyl radicals, which are the main oxidants of cell membranes (Hu et al., 2017). Malonaldehyde is a lipid aldehyde produced by cell membrane disruption, widely used as an indicator of cell damage (Morales and Bosh 2019).

Conclusion

In summary, this study provides a definitive, mechanics driven resolution to the challenge of low-mobility iron delivery in agroecosystems, effectively bridging the gap between advanced nanomaterial engineering and environmental safety boundaries. Our structural and thermal characterizations confirm that the chitosan matrix successfully encapsulates the magnetite core, yielding stable CS:Fe_3O_4 NPs while preventing large-scale colloidal aggregation and structurally modulating iron-ion availability. Crucially, the biological datasets obtained herein establish a robust, concentration-dependent hormetic paradigm in *Zea mays* L. tissues, successfully mapping the precise metabolic threshold where nano-iron transits from a physiological stimulant to a severe ecotoxin. Within the biostimulatory window, spanning from 20 (200) to 60 (600), µg mg^{-1} (µg L^{-1}), the datasets demonstrate a synchronized upregulation of photosynthetic pigment biosynthesis and electron transport efficiency, unlocking a highly optimized state of chloroplast bioenergetics. Conversely, extending exposure levels beyond the 80 (800) µg mg^{-1} (µg L^{-1}) inflection point triggers a severe biological collapse characterized by acute phytotoxicity. At this elevated threshold, the sudden, exponential accumulation of hydrogen peroxide overpowers the tissue's non-enzymatic defense pool evidenced by a critical depletion of total phenolics, flavonoids, and tannins and directly induces catastrophic lipid peroxidation of the plasma membranes, as validated by high malondialdehyde levels. Our biochemical profiling resolves that under this acute oxidative stress, the plant tissue relies dynamically on a catalase-mediated pathway as its primary enzymatic barrier to mitigate iron-induced reactive oxygen species and delay systemic cellular necrosis. The broader scientific contribution of this work extends far beyond standard crop nutrition, providing the global scientific community with critical, quantifiable baseline parameters required to establish regulatory environmental ceilings for engineered agro-nanomaterials. By demonstrating that a strict safety limit must be maintained below 60 (600) µg mg^{-1} (µg L^{-1}) to avoid cellular damage, these findings deliver a functional template for Safe-by-design precision nanoformulations. This contribution is indispensable for mitigating ecological risks, preventing non-target soil and aquatic chemical runoff, and ensuring that the transition toward nano-enabled sustainable agriculture is both highly productive and ecologically secure.

Declarations

Ethics declaration: not applicable

"This study was financed in part by the Coordenação de Aperfeiçoamento de Pessoal de Nível Superior - Brasil (CAPES) - Finance Code 001"

Declaration of interests

 The authors declare that they have no known competing financial interests or personal relationships that could have appeared to influence the work reported in this paper.
 The authors declare the following financial interests/personal relationships which may be considered as potential competing interests:

Author Contribution

Simone Yasuda Fernandes Investigation, formal analysis, writing (original draft), visualization and editing.Montcharles Silva Pontes Review & editing.Jaqueline da Silva Santos Review & editing.Gilberto José de Arruda Conceptualization, investigation, analysis, review & editing.Etenaldo Felipe Santiago Supervision, review & editing.

Acknowledgement

This study was partially funded by the Coordenação de Aperfeiçoamento de Pessoal de Nível Superior – Brasil (CAPES) – Financial Code 001. In addition, we thank FAPESP (Process No. 2022/00045–3), CNPq, and FUNDECT on behalf of the co-authors.

Data Availability

All data supporting the findings of this study are available within the paper.

References

1. Ahmed, M. A., Shafiei-Masouleh, S. S., Mohsin, R. M., Salih, Z. K. (2023). Foliar application of iron oxide nanoparticles promotes growth, mineral contents, and medicinal qualities of *Solidago virgaurea* L. Journal of Soil Science and Plant Nutrition, v. 23(2), p. 2610–2624. https://doi.org/10.1007/s42729-023-01218-2.
2. Alexieva, V., Sergiev, I., Mapelli, S., Karanov, E. (2001). The effect of drought and ultraviolet radiation on growth and stress markers in pea and wheat. Plant, Cell & Environment, v. 24(12), p. 1337–1344. https://doi.org/10.1046/j.1365-3040.2001.00778.x.
3. Ansari, A., Vahedi, S., Tavakoli, O., Khoobi, M., Faramarzi, M. A. (2019). Novel Fe_3O_4/hydroxyapatite/β-cyclodextrin nanocomposite adsorbent: synthesis and application in heavy metal removal from aqueous solution. Applied Organometallic Chemistry, v. 33(1), p. 4634. https://doi.org/10.1002/aoc.4634.
4. Anuta, V., Blidaru, A., Dinu-Pîrvu, C.-E., Fierascu, R. C., Fierascu, I., Toma, D. I., Popa, L., Ghica, M. V., Prisada, R. M. (2025). Metal-based nanoparticles with biostimulatory effects: harnessing

nanotechnology for enhanced agricultural sustainability. Materials, v. 18, p. 3142. https://doi.org/10.3390/ma18133142.

5. Apel, K., Hirt, H. (2004). Reactive oxygen species: metabolism, oxidative stress, and signal transduction. Annu. Rev. Plant Biol. v. 55, p. 373–399. https://doi.org/10.1146/annurev.arplant.55.031903.141701.
6. Ates, B., Ulu, A., Köytepe, S., Noma, S. A. A., Kolat, V. S., Izgi, T. (2018). Magnetic-propelled Fe_3O_4–chitosan carriers enhance L-asparaginase catalytic activity: a promising strategy for enzyme immobilization. RSC advances, v. 8(63), p,. 36063–36075. https://doi.org/10.1039/C8RA06346J.
7. Ba-Abbad, M. M., Benamour, A., Ewis, D., Mohammad, A. W., Mahmoudi, E. (2022). Synthesis of Fe_3O_4 nanoparticles with different shapes through a co-precipitation method and their application. Jom, v. 74(9), p. 3531–3539. https://doi.org/10.1007/s11837-022-05380-3.
8. Baranowska, A. (2023). The nutritional value and health benefits of sweet corn kernels (*Zea mays* ssp. saccharata). Health Problems of Civilization, v. 17(4), p. 408–416. https://doi.org/10.5114/hpc.2023.133364.
9. Van Bavel, N., Issler, T., Pang, L., Anikovskiy, M., Prenner, E. J. (2023). A simple method for synthesis of chitosan nanoparticles with ionic gelation and homogenization. Molecules, v. 28, p. 4328. https://doi.org/10.3390/molecules28114328.
10. Deng, C., Tang, Q., Yang, Z., Dai, Z., Cheng, C., Xu, Y., Chen, X., Zhang, X., Su, J. (2022). Effects of iron oxide nanoparticles on phenotype and metabolite changes in hemp clones (*Cannabis sativa* L.). Frontiers of Environmental Science & Engineering, v. 16(10), p. 134. Front. https://doi.org/10.1007/s11783-022-1569-9.
11. Dey, S. C., Al-Amin, M., Rashid, T. U., Sultan, M. Z., Ashaduzzaman, M., Sarker, M., Shamsuddin, S. M. (2016). Preparation, characterization and performance evaluation of chitosan as an adsorbent for remazol red. Int. J. Latest Res. Eng. Technol, v. 2(2), p. 52–62.
12. Elanchezhian, R., Kumar, D., Ramesh, K., Biswas, A. K., Guhey, A., Patra, A. K. (2017). Morpho-physiological and biochemical response of maize (*Zea mays* L.) plants fertilized with nano-iron (Fe_3O_4) micronutrient. Journal of Plant Nutrition, v. 40(14), p. 1969–1977. https://doi.org/10.1080/01904167.2016.1270320.
13. Eldeeb, B. A., El-Raheem, W. M. A., Elbeltagi, S. (2023). Green synthesis of biocompatible Fe_3O_4 magnetic nanoparticles using Citrus sinensis peels extract for their biological activities and magnetic-hyperthermia applications. Scientific Reports, v. 13(1), p. 19000. https://doi.org/10.1038/s41598-023-46287-6.
14. Feng, Y., Kreslavski, V. D., Shmarev, A. N., Ivanov, A. A., Zharmukhamedov, S. K., Kosobryukhov, A., Yu, M., Allakhverdiev, S. I., Shabala, S. (2022). Effects of iron oxide nanoparticles (Fe3O4) on growth, photosynthesis, antioxidant activity and distribution of mineral elements in wheat (*Triticum aestivum*) Plants. Plants, v. 11(14), p. 1894. https://doi.org/10.3390/plants11141894.
15. Food and Agriculture Organization of the United Nations - FAO. (2024). Food Outlook – Biannual report on global food markets. Food Outlook, June 2024. Rome.

16. Fumis, D. B., Silveira, M. L., Gaglieri, C., Ferreira, L. T., Marques, R. F., & Magdalena, A. G. (2022). The effect of EDTA functionalization on Fe_3O_4 thermal behavior. Materials Research, v. 25, p. 202–312. https://doi.org/10.1590/1980-5373-MR-2022-0312.
17. Gamito, G., Monteiro, C. J., Dias, M. C., Oliveira, H., Silva, A. M., Faustino, M. A., Silva, S. (2024). Impact of Fe_3O_4-porphyrin hybrid nanoparticles on wheat: Physiological and metabolic advance. Journal of Hazardous Materials, v. 471, p. 134–243. https://doi.org/10.1016/j.jhazmat.2024.134243.
18. Giannopolitis, C. N., Ries, S. K. (1977). Superoxide dismutases: I. Occurrence in higher plants. Plant Physiol. V. 59, p. 309–314.
19. Guibal, E., Touraud, E., Roussy, J. (2005). Chitosan interactions with metal ions and dyes: dissolved-state vs. solid-state application. Journal of Microbiology & Biotechnology, v. 21, p. 913–920. http://doi.org/10.1007/s11274-004-6559-5.
20. Grillo, R., Gallo, J., Stroppa, D. G., Carbó-Argibay, E., Lima, R., Fraceto, L. F., Bañobre-López, M. (2016). Sub-micrometer magnetic nanocomposites: insights into the effect of magnetic nanoparticles interactions on the optimization of SAR and MRI performance. ACS Applied Materials & Interfaces, v. 8(39), p. 777–787. https://doi.org/10.1021/acsami.6b08663.
21. Haris, M., Hussain, T., Mohamed, H. I., Khan, A., Ansari, M. S., Tauseef, A., Khan, A. A., Akhtar, N. (2023). Nanotechnology–A new frontier of nano-farming in agricultural and food production and its development. Science of The Total Environment, v. 857, p. 159–639. https://doi.org/10.1016/j.scitotenv.2022.159639.
22. Haydar, M. S., Ghosh, S., Mandal, P. (2021). Application of iron oxide nanoparticles as micronutrient fertilizer in mulberry propagation. Journal of Plant Growth Regulation, p. 1–21. https://doi.org/10.1007/s00344-021-10413-3.
23. Hu Jing, H. J., Guo HuiYuan, G. H., Li JunLi, L. J., Gan QiuLiang, G. Q., Wang YunQiang, W. Y., Xing BaoShan, X. B. (2017). Comparative impacts of iron oxide nanoparticles and ferric ions on the growth of *Citrus maxima*. Environ Pollut, v. 221, p. 199–208. https://doi.org/10.1016/j.envpol.2016.11.064.
24. Huseyin Tombuloglu, H. T., Yassine Slimani, Y. S., Guzin Tombuloglu, G. T., Munirah Almessiere, M. A., Abdulhadi Baykal, A. B. (2019). Uptake and translocation of magnetite (Fe_3O_4) nanoparticles and its impact on photosynthetic genes in barley (*Hordeum vulgare* L.). Chemosphere, v. 226, p. 110–122. https://doi.org/10.1016/j.chemosphere.2019.03.075.
25. Kalisz, A., Húska, D., Jurkow, R., Dvořák, M., Klejdus, B., Caruso, G., Sękara, A. (2021). Nanoparticles of cerium, iron, and silicon oxides change the metabolism of phenols and flavonoids in butterhead lettuce and sweet pepper seedlings. Environmental Science: Nano, v. 8(7), p. 1945–1959. http://doi.org/10.1039/d1en00262g.
26. Kejík, Z., Kaplánek, R., Masařík, M., Babula, P., Matkowski, A., Filipenský, P., Veselá, K., Gburek, J., Sýkora, D., Martásek, P., Jakubek, M. (2021). Iron complexes of flavonoids-antioxidant capacity and beyond. International journal of molecular sciences, v. 22(2), p. 646. https://doi.org/10.3390/ijms22020646.

27. Kobayashi, T., Nozoye, T., Nishizawa, N. K. (2019). Iron transport and its regulation in plants. Free Radical Biology and Medicine, v.133, p. 11–20. https://doi.org/10.1016/j.freeradbiomed.2018.10.439.
28. Kraus, T. E., McKersie, B. D., Fletcher, R. A. (1995). Paclobutrazol-induced tolerance of wheat leaves to paraquat may involve increased antioxidant enzyme activity. Journal of Plant Physiology, v. 145(4), p. 570–576.
29. Larsen, A. E., Claire Powers, L., McComb, S. (2021). Identifying and characterizing pesticide use on 9.000 fields of organic agriculture. Nature communications, v. 12(1), p. 5461. https://doi.org/10.1038/s41467-021-25502-w.
30. Li, J., Cao, X., Jia, X., Liu, L., Cao, H., Qin, W., Li, M. (2021). Iron deficiency leads to chlorosis through impacting chlorophyll synthesis and nitrogen metabolism in Areca catechu L. Frontiers in Plant Science, v. 12, p. 71–93. https://doi.org/10.3389/fpls.2021.710093.
31. Li, P., Wang, A., Du, W., Mao, L., Wei, Z., Wang, S., Yuan, H., Ji, R., Zhao, L. (2020). Insight into the interaction between Fe-based nanomaterials and maize (*Zea mays*) plants at metabolic level. Science of the Total Environment, v. 738, p. 139–195. https://doi.org/10.1016/j.scitotenv.2020.139795.
32. Liu, J., Zhang, D., Bao, L., Mao, T., Zhao, L., Liu, C., Huang, G., Zhai, Y. (2024). Plant nanobiotechnology: a new strategy to enhance crop photosynthesis. Environmental Science: Nano. v. 11, p. 4655–4665. https://doi.org/10.1039/D4EN00520A.
33. Lichtenthaler, H. K., Wellburn, A. R. 1983. Determinations of total carotenoids and chlorophylls a and b of leaf extracts in different solvents. Transactions, v. 603, p. 591–592.
34. Lin, J. Y., Tang, C. Y. (2007). Determination of total phenolic and flavonoid contents in selected fruits and vegetables, as well as their stimulatory effects on mouse splenocyte proliferation. Food Chemistry, v. 101, p. 140–147, https://doi.org/10.1016/j.foodchem.2006.01.014.
35. Lustriane, C., Dwivany, F. M., Suendo, V., Reza, M. (2018). Effect of chitosan and chitosan-nanoparticles on post harvest quality of banana fruits. Journal of Plant Biotechnology, v. 45(1), p. 36–44. https://doi.org/10.5010/JPB.2018.45.1.036.
36. Madhupriyaa, D., Baskar, M., Sherene Jenita Rajammal, T., Kuppusamy, S., Rathika, S., Umamaheswari, T., Mohanapragash, A. G. (2024). Efficacy of chelated micronutrients in plant nutrition. Communications in Soil Science and Plant Analysis, p. 1–24. https://doi.org/10.1080/00103624.2024.2397019.
37. Magdalena, A. G., Silva, I. M. B., Marques, R. F. C., Pipi, A. R. F., Lisboa-Filho, P. N., Jafelicci Jr, M. (2018). EDTA-functionalized Fe_3O_4 nanoparticles. Journal of Physics and Chemistry of Solids, v. 113, p. 5–10. https://doi.org/10.1016/j.jpcs.2017.10.002.
38. Matsuno, H.; Uritani, I. (1972). Physiological behavior of peroxidase isozymes in sweet potato root tissue injured by cutting or with black rot. Plant and Cell Physiology, v.13, p.1091–1101.
39. Merino-Treviño, M., Morales-Cepeda, A. B., Peraza-Vázquez, A., Onofre-Bustamante, E. (2024). Plants with silver nanoparticles to improve electrical conductivity: an innovative approach in biology. International Journal of Environmental Science and Technology, v. 22, p. 1–12. http://doi.org/10.1007/s13762-024-05837-9.

40. Moldes, C. A., Medici, L. O., Abrahao, O. S., Tsai, S. M., Azevedo, R. A. (2008). Biochemical responses of glyphosate resistant and susceptible soybean plants exposed to glyphosate. Acta Physiologiae Plantarum, v. 30(4), p. 469–479. http://doi.org/10.1007/s11738-008-0144-8.

41. Morales, M., Munné-Bosch, S. (2019). Malondialdehyde: facts and artifacts. Plant physiology, v. 180(3), p. 1246–1250. https://doi.org/10.1104/pp.19.00405.

42. Müller, C., Kuki, K. N., Pinheiro, D. T., de Souza, L. R., Siqueira Silva, A. I., Loureiro, M. E., Almeida, A. M. (2015). Differential physiological responses in rice upon exposure to excess distinct iron forms. Plant and Soil, v. 391, p. 123–138. https://doi.org/10.1007/s11104-015-2405-9.

43. Nam, Y. S., Park, W. H., Ihm, D., Hudson, S. M. (2010). Effect of the degree of deacetylation on the thermal decomposition of chitin and chitosan nanofibers. Carbohydrate Polymers, v. 80(1), p. 291–295. http://doi.org/10.1016/j.carbpol.2009.11.030.

44. Nguyen, M. D., Tran, H. V., Xu, S., Lee, T. R. (2021). Fe3O4 nanoparticles: structures, synthesis, magnetic properties, surface functionalization, and emerging applications. Applied Sciences, v. 11(23), p. 11301. https://doi.org/10.3390/app112311301.

45. Pansera, M. R., Santos, A. C. A., Paese, K., Wasum, R., Rossato, M., Rota, L. D., Pauletti, G. F., Serafini, L. A. (2003). Análise de taninos totais em plantas aromáticas e medicinais cultivadas no Nordeste e Rio Grande do Sul. Revista Brasileira de Farmacologia, p. 102–115.

46. Pereira, F. S., Lanfredi, S., González, E. R. P., da Silva Agostini, D. L., Gomes, H. M., dos Santos Medeiros, R. (2017). Thermal and morphological study of chitosan metal complexes. Journal of Thermal Analysis and Calorimetry, v. 129(1), p. 291–301. http://doi.org/10.1007/s10973-017-6146-2.

47. Pontes, M. S., Antunes, D. R., Oliveira, I. P., Forini, M. M., Santos, J. S., Arruda, G. J., Grillo, R. (2021). Chitosan/tripolyphosphate nanoformulation carrying paraquat: insights on its enhanced herbicidal activity. Environmental Science: Nano, v. 8(5), p. 1336–1351. https://doi.org/10.1039/D0EN01128B.

48. Pontes, M. S., Santos, J. S., da Silva, J. L., Miguel, T. B., Miguel, E. C., Souza Filho, A. G., Sandro, L., Arruda, G., Felipe Santiago, E. (2023). Assessing the fate of superparamagnetic iron oxide nanoparticles carrying usnic acid as chemical cargo on the soil microbial community. ACS nano, v. 17(8), p. 7417–7430. https://doi.org/10.1021/acsnano.2c11985.

49. Pontes, M. S., Araujo, L. O., Santos, J. S., da Silva, J. L., Miguel, T. B., Miguel, E. C., F. Santiago, E. (2025). targeted inhibition of photosystem ii electron transport using bioherbicide-loaded ultrasmall nanodevices. ACS Omega. v. 17;10(46), p. 55733–55749. https://doi.org/10.1021/acsomega.5c07085.

50. Qiu, H., Cui, B., Li, G., Yang, J., Peng, H., Wang, Y., Li, N., Gao, R., Chang, Z., Wang, Y. (2014). Novel Fe_3O_4@ ZnO@ $mSiO_2$ nanocarrier for targeted drug delivery and controllable release with microwave irradiation. The Journal of Physical Chemistry C, v. 118(27), p. 14929–14937. https://doi.org/10.1021/jp502820r.

51. Rahman, L., Goswami, J., Choudhury, D. (2022). Assessment of physical and thermal behaviour of chitosan-based biocomposites reinforced with leaf and stem extract of *Tectona grandis*. Polymers and Polymer composites, v. 30, p. 196–219. https://doi.org/10.1177/09673911221076305.

52. Santos, J. S., Pontes, M. S., Azevedo, R. A. (2025). Nanoformulations in agriculture food safety vs environmental safety. Trends in Plant Science. http://doi.org/10.1016/j.tplants.2025.05.016.
53. Şahin, M., Arslan, Y., Tomul, F. (2022). Adsorption, oxidation, kinetic and thermodynamic studies of methyl orange by magnetic Fe_3O_4 NPs and their chitosan/alginate nanocomposites. International Journal of Environmental Analytical Chemistry, p. 1–20. https://doi.org/10.1080/03067319.2022.2140417.
54. Sanders, J., Gallagher, P. (2003). Kinetics of the oxidation of magnetite using simultaneous TG/DSC. Journal of Thermal Analysis and Calorimetry, v. 72(3), p. 777–789.
55. Silveira, M. L. D. C., Silva, I. M. B., Magdalena, A. G. (2021). Synthesis and characterization of Fe_3O_4 -NH_2 and Fe_3O_4 -NH_2 chitosan nanoparticles. Cerâmica, v. 31(2), p. 295–300. http://dx.doi.org/10.1590/0366-69132021673833101.
56. Schmidt, S. B., Eisenhut, M., Schneider, A. (2020). Chloroplast transition metal regulation for efficient photosynthesis. Trends in Plant Science, v. 25(8), p. 817–828. https://doi.org/10.1016/j.tplants.2020.03.003.
57. Shirsat, S., Suthindhiran, K. (2023). Iron oxide nanoparticles as iron micronutrient fertilizer—Opportunities and limitations. Journal of Plant Nutrition and Soil Science, v. 187, p. 565–588. https://doi.org/10.1002/jpln.202300203.
58. Strasser, R. J.; Tsimilli-Michael, M.; Srivastava, A. (2004). Analysis of the chlorophyll a. Fluorescence Transient, p. 321– 362. https://doi.org/10.1007/978-1-4020-3218-9_12.
59. Tsiepe, J. T., Mamba, B. B., Inamuddin, Abd-El-Aziz, A. S., Mishra, A. K. (2018). Fe3O4–β-cyclodextrin–chitosan bionanocomposite for arsenic removal from aqueous solution. Journal of Inorganic and Organometallic Polymers and Materials, v. 28(2), p. 467–480. http://doi.org/10.1007/s10904-017-0741-3.
60. Villar, C. M. M., Domínguez, J. C., Alonso, M. V., Oliet, M., Rodriguez, F. (2018). Thermal and kinetics of the degradation of chitosan with different deacetylation degrees under oxidizing atmosphere. Thermochimica Acta, v. 670, p. 18–26. http://doi.org/10.1016/j.tca.2018.10.004.
61. Wang, Y., Wang, S., Xu, M., Xiao, L., Dai, Z., Li, J. (2019). The impacts of γ-Fe_2O_3 and Fe_3O_4 nanoparticles on the physiology and fruit quality of muskmelon (Cucumis melo) plants. Environmental pollution, v. 249, p. 1011–1018. http://doi.org/10.1016/j.envpol.2019.03.119.
62. Wujcicki, L., Kluczka, J. (2026). Ion-imprinted chitosan technology for heavy metal ion removal from water and wastewater: a review on recent insights and future perspectives. Journal of Molecular Sciences, v. 27(7), p. 3183. https://doi.org/10.3390/ijms27073183.
63. Zhang, Y., Goss, G. G. (2022). Nanotechnology in agriculture: Comparison of the toxicity between conventional and nano-based agrochemicals on non-target aquatic species. Journal of Hazardous Materials, v. 439, p. 129–559. http://doi.org/10.1016/j.jhazmat.2022.129559.
64. Zuluaga, M. Y. A., Cardarelli, M., Rouphael, Y., Cesco, S., Pii, Y., Colla, G. (2023). Iron nutrition in agriculture: From synthetic chelates to biochelates. Scientia Horticulturae, v. 312, p. 111–133. http://doi.org/10.1016/j.scienta.2023.111833.

65. Yang, M., Zhou, D., Hang, H., Chen, S., Liu, H., Su, J., Zhao, G. (2024). Effects of balancing exchangeable cations Ca, Mg, and K on the growth of tomato seedlings (*Solanum lycopersicum* L.) based on increased soil cation exchange capacity. Agronomy, v. 14(3), p. 629. https://doi.org/10.3390/agronomy14030629.

Figures

Figure 1

Representative diagram of the synthesis and chemical groups involved in the interaction of chitosan with Fe_3O_4 NPs.

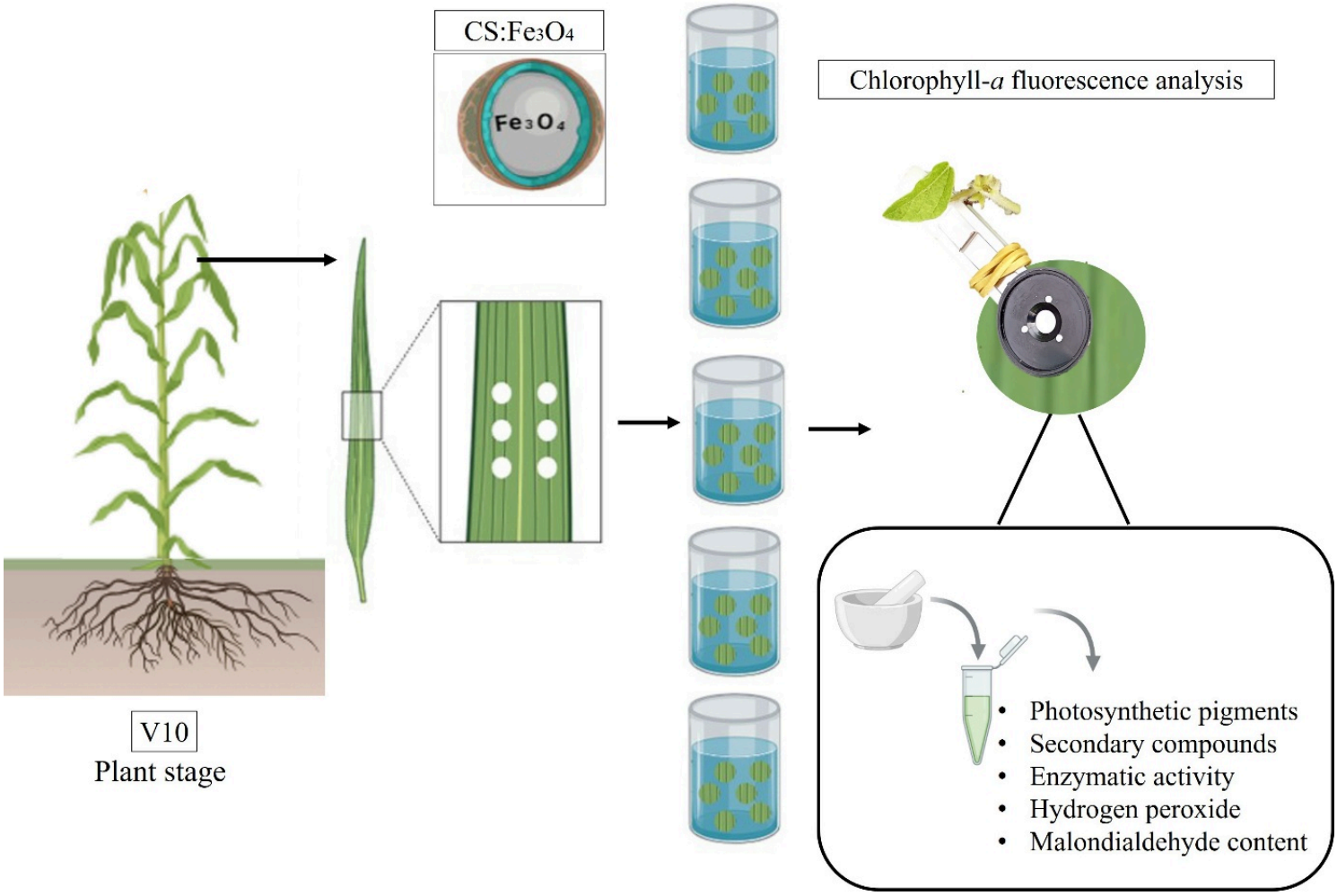

Figure 2

Representation of the experiment by immersing *Zea mays* L. leaf discs in solutions of CS and CS:Fe_3O_4NPs.

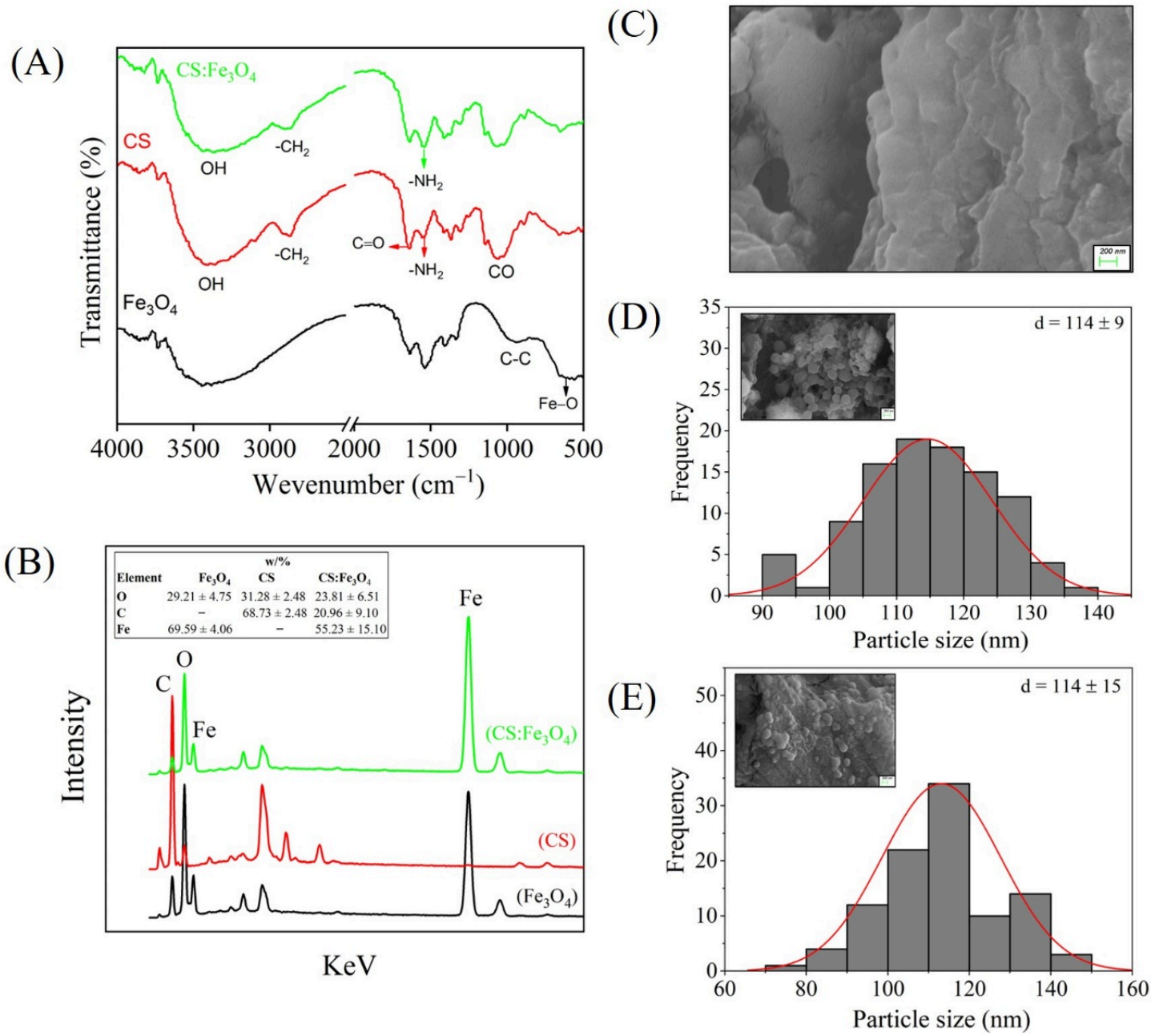

Figure 3

Characterization: FTIR spectroscopy (A). Elemental analysis – EDS (B). Scanning microscopy of CS (C), Fe_3O_4 NPs (D), CS:Fe_3O_4 NPs (E) and (F-H) their respective size distribution histograms.

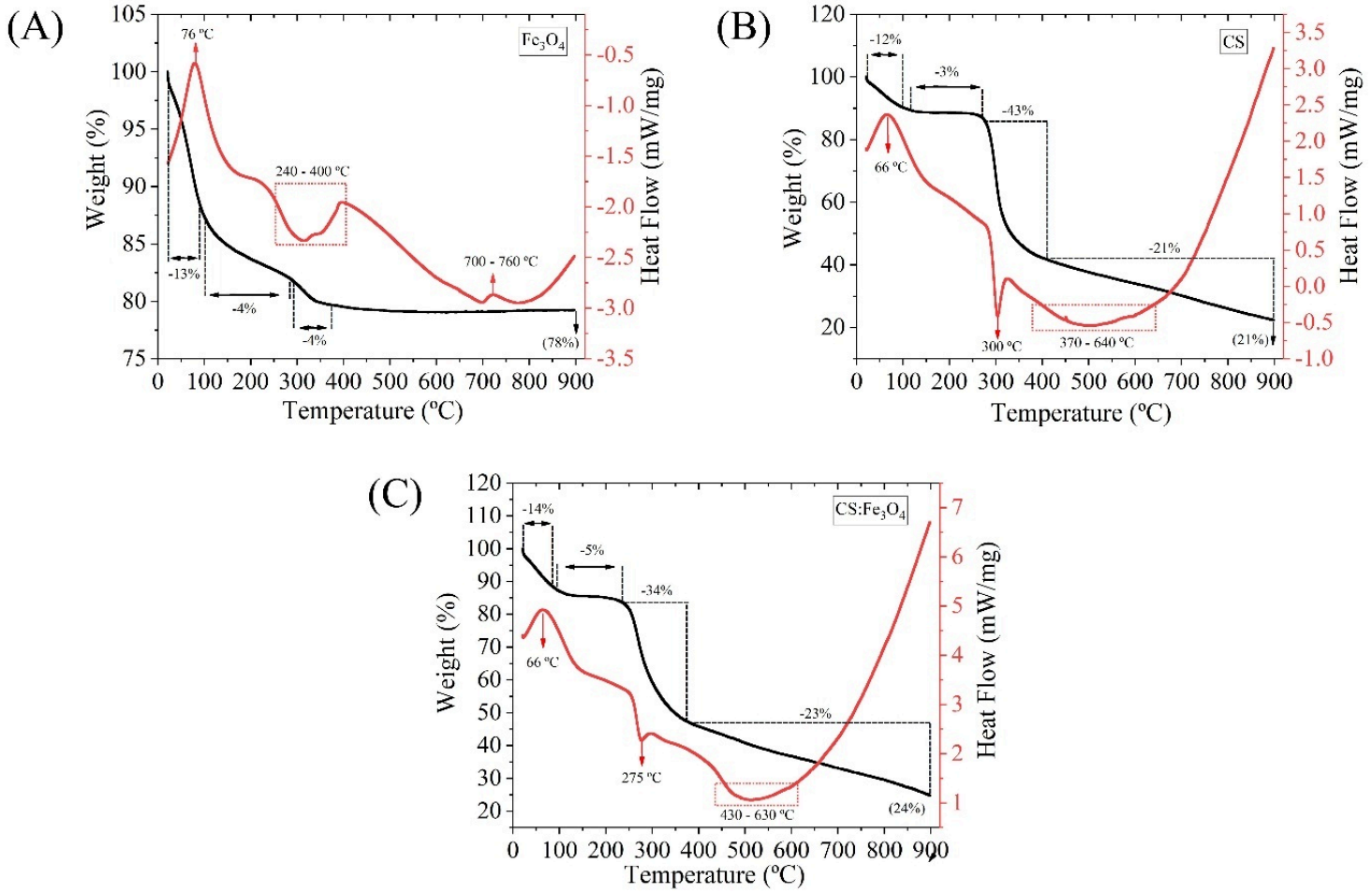

Figure 4

DTA/DSC thermograms of Fe_3O_4 NPs (A), CS (B) and CS:Fe_3O_4 NPs (C).

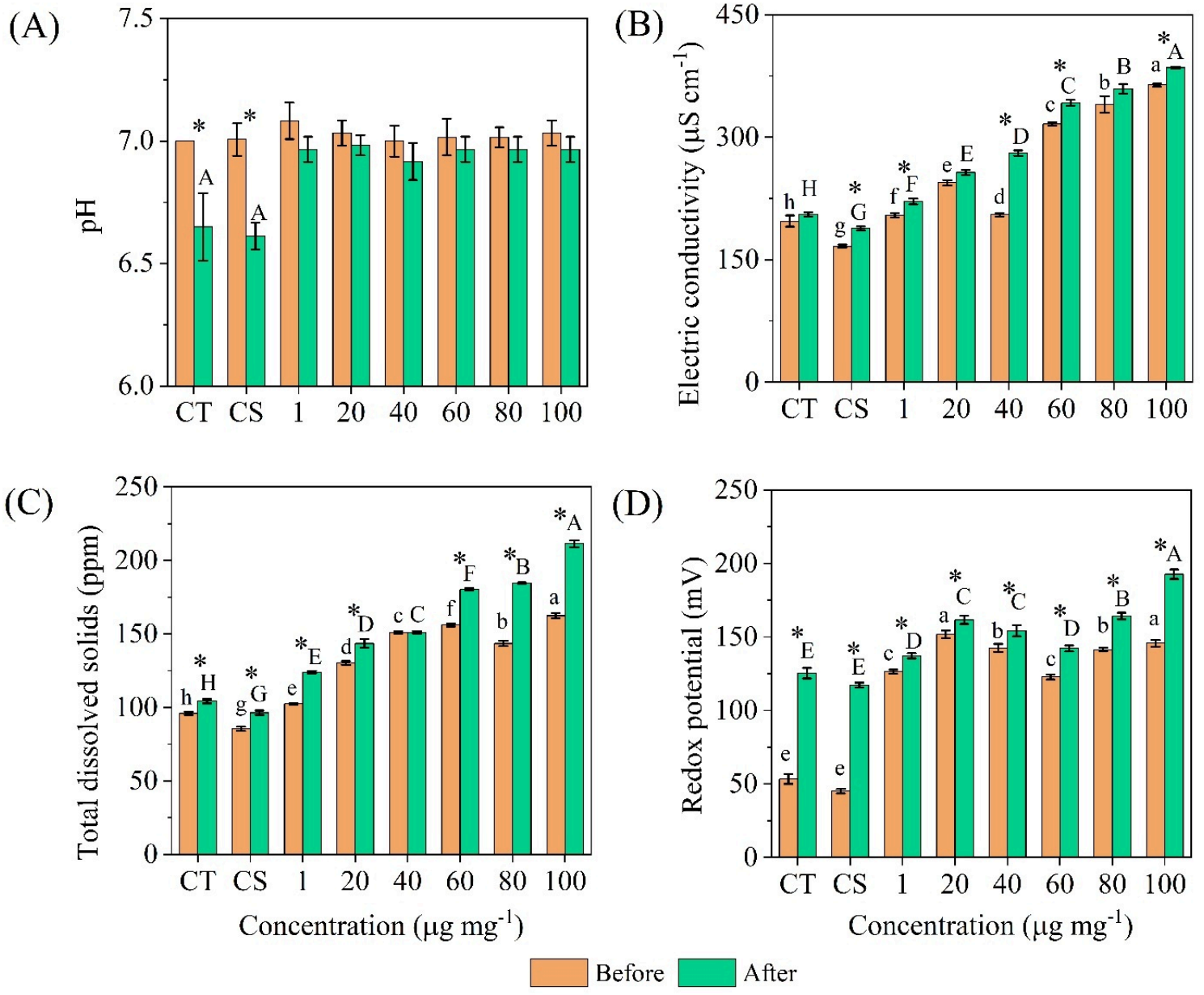

Figure 5

Chemical parameters of solutions with *Zea mays* leaf discs before and after 24 hours of treatment with CS and CS:Fe_3O_4 NPs. pH (A). Electrical conductivity (B). Total dissolved solids (C). Oxidation-reduction potential (D). Results are represented by means followed by standard deviation (±). Different lowercase letters indicate a significant difference ($p < 0.05$) between the treatments. Different uppercase letters indicate a significant difference ($p < 0.05$) between the treatments after 24 hours. The symbol * between columns of the same treatment indicate a significant difference ($p < 0.05$) before and after 24 hours.

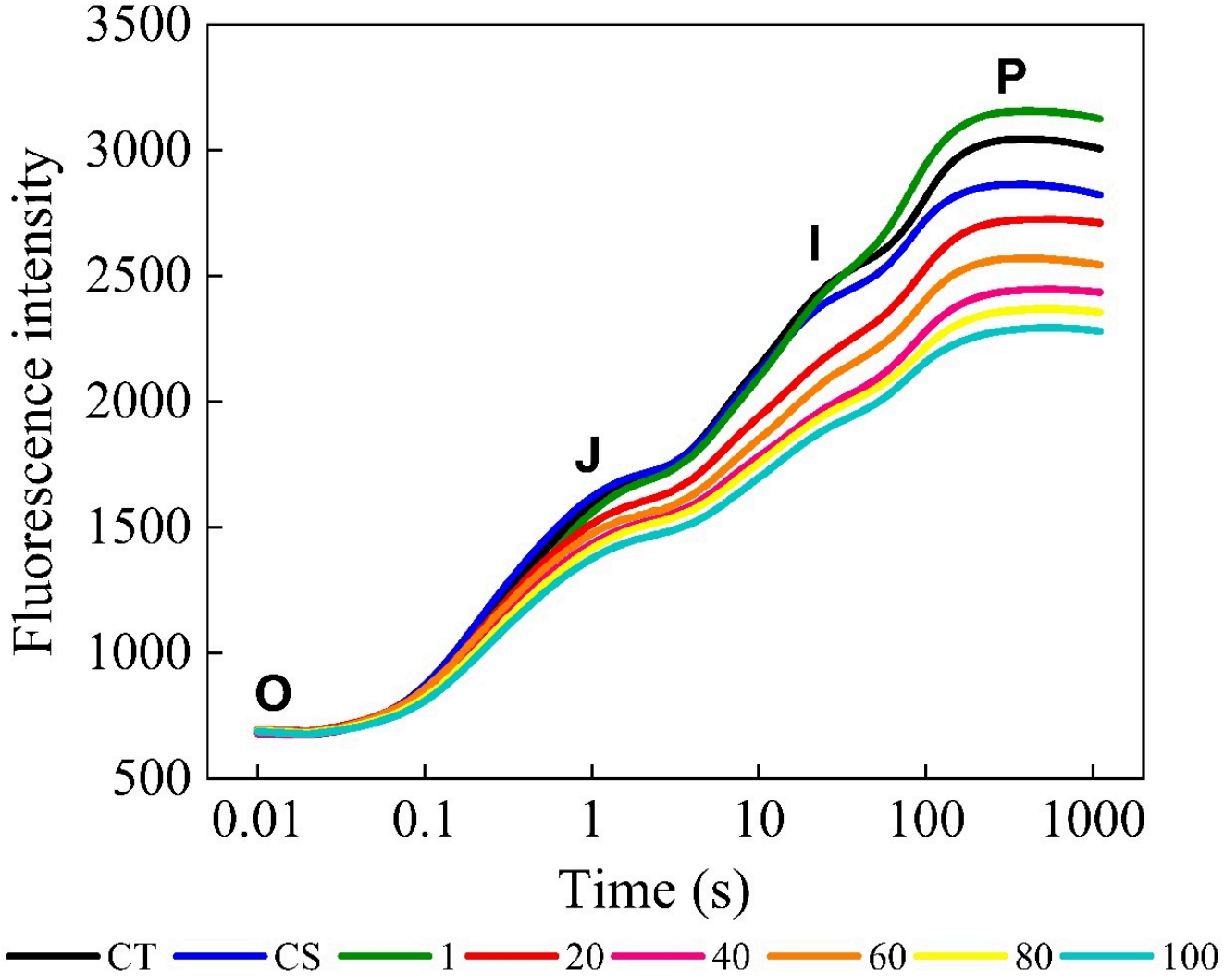

Figure 6

OJIP transient curve. Effect of CS and CS:Fe_3O_4 NPs.

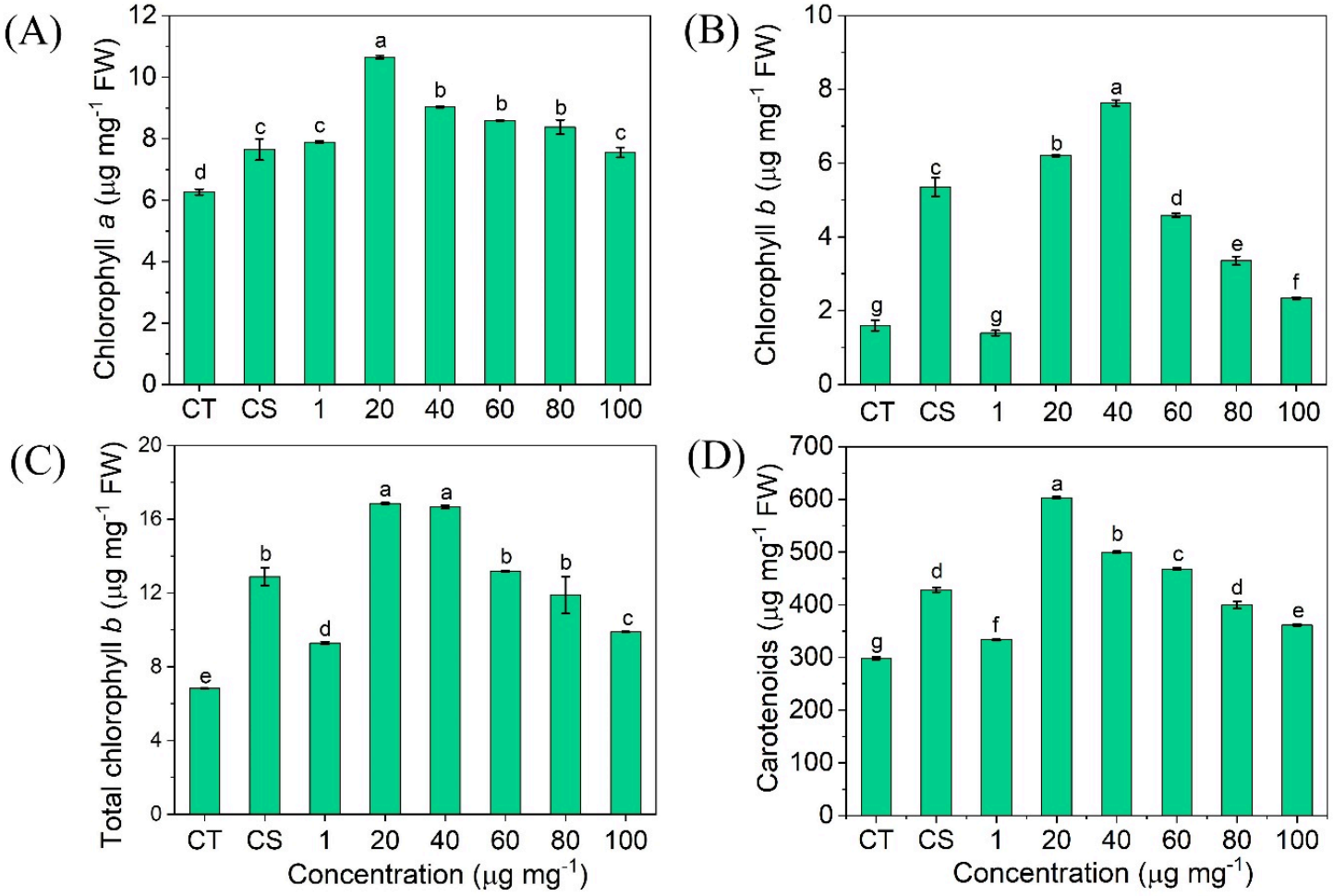

Figure 7

Effect of CS and CS:Fe_3O_4 NPs on photosynthetic pigment content. Chlorophyll *a* (A). Chlorophyll *b* (B). Total chlorophyll (C). Carotenoids (D). Significant differences ($p < 0.05$) are represented by different letters between treatments. Data are represented by the mean followed by the standard deviation (±).

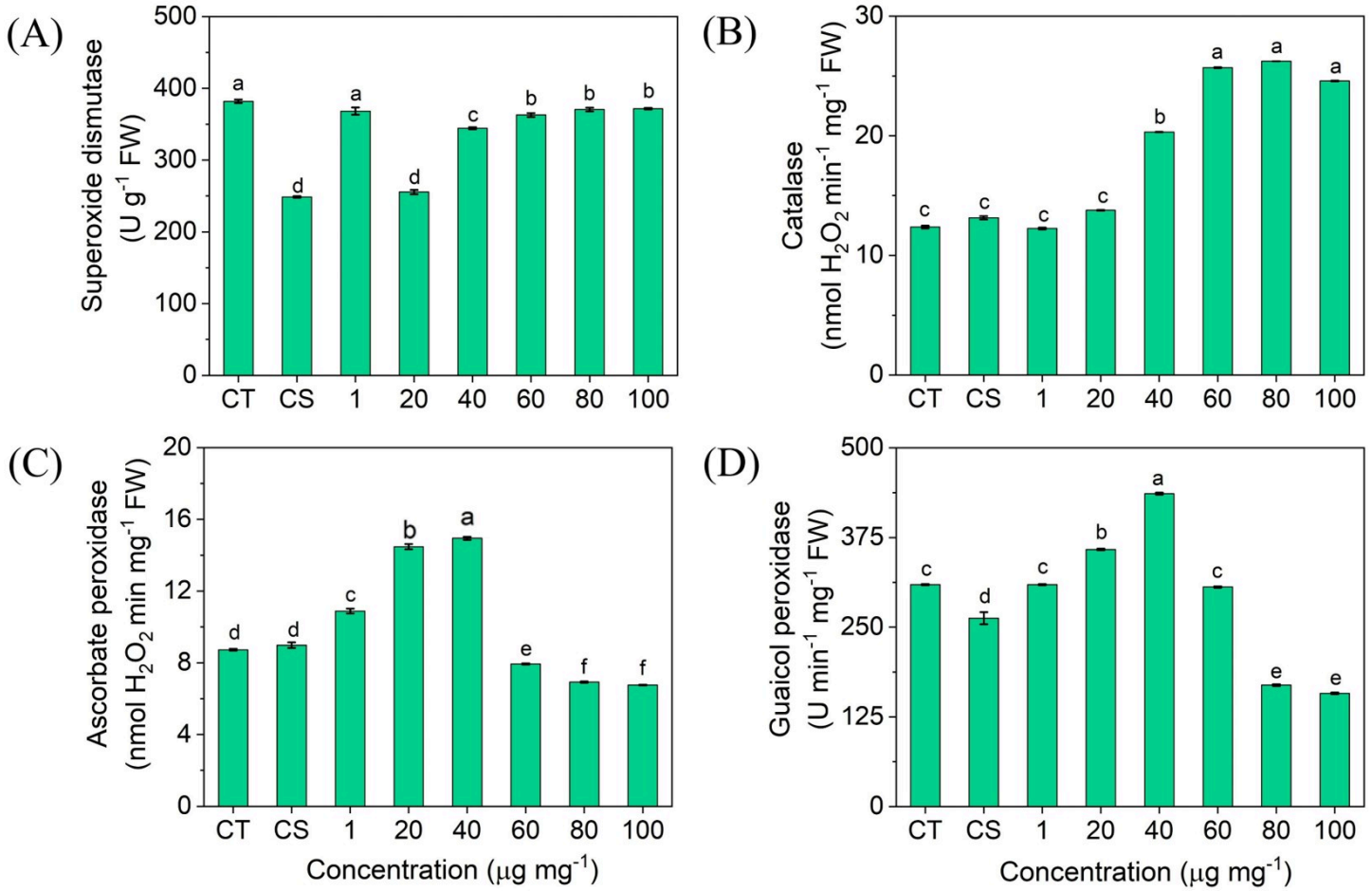

Figure 8

Effect of CS and CS:Fe_3O_4 NPs on the enzymatic activity of Superoxide dismutase (A). Catalase (B). Ascorbate peroxidase (C). Guaicol peroxidase (D). Significant differences ($p < 0.05$) are represented by different letters between treatments. Data are represented by the mean followed by the standard deviation (±).

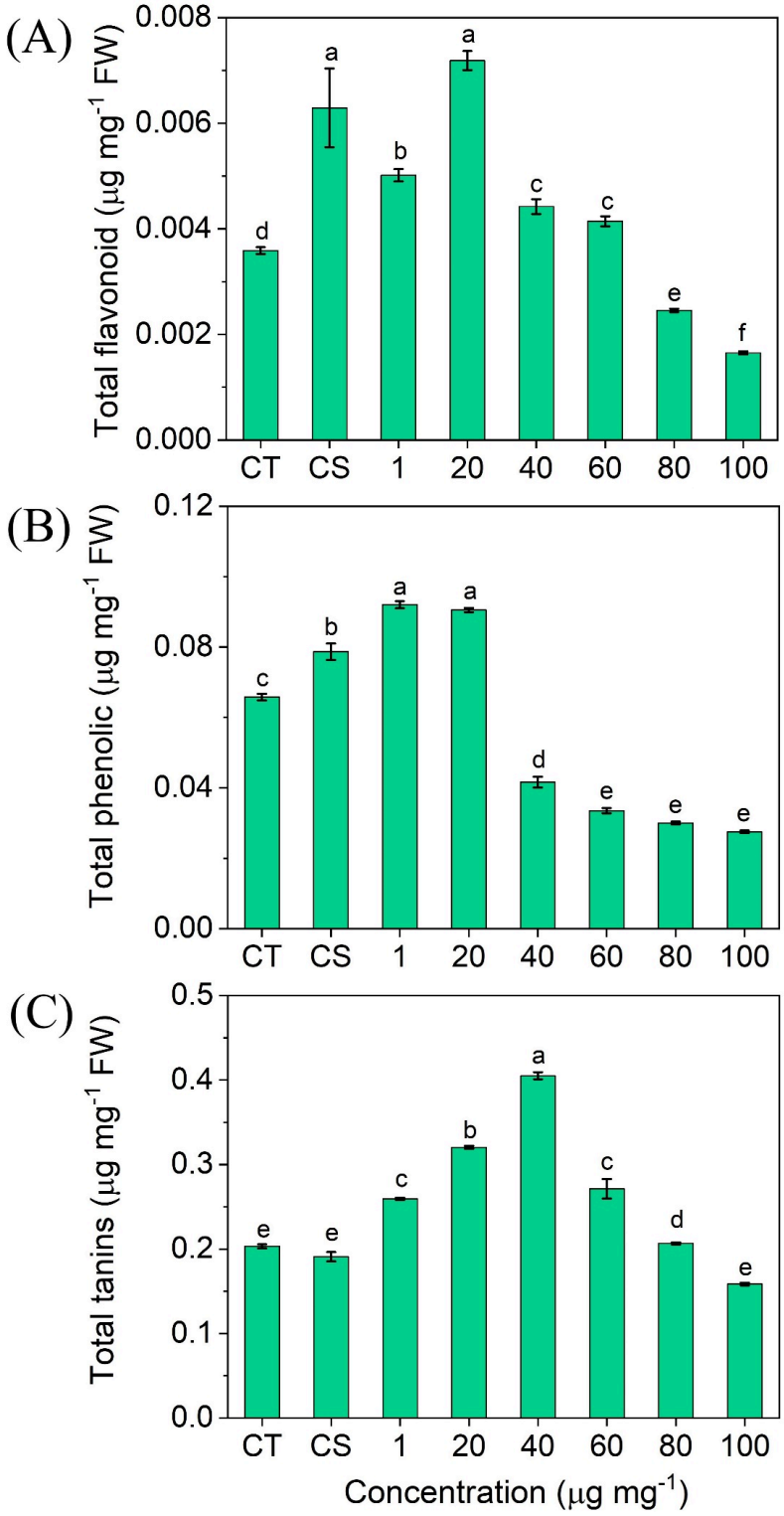

Figure 9

Effect of CS and CS:Fe_3O_4 NPs on the content of flavonoids (A). Phenolics (B). Tannins (C). Significant differences ($p < 0.05$) are represented by different letters between treatments. Data are represented by the mean followed by the standard deviation (±).

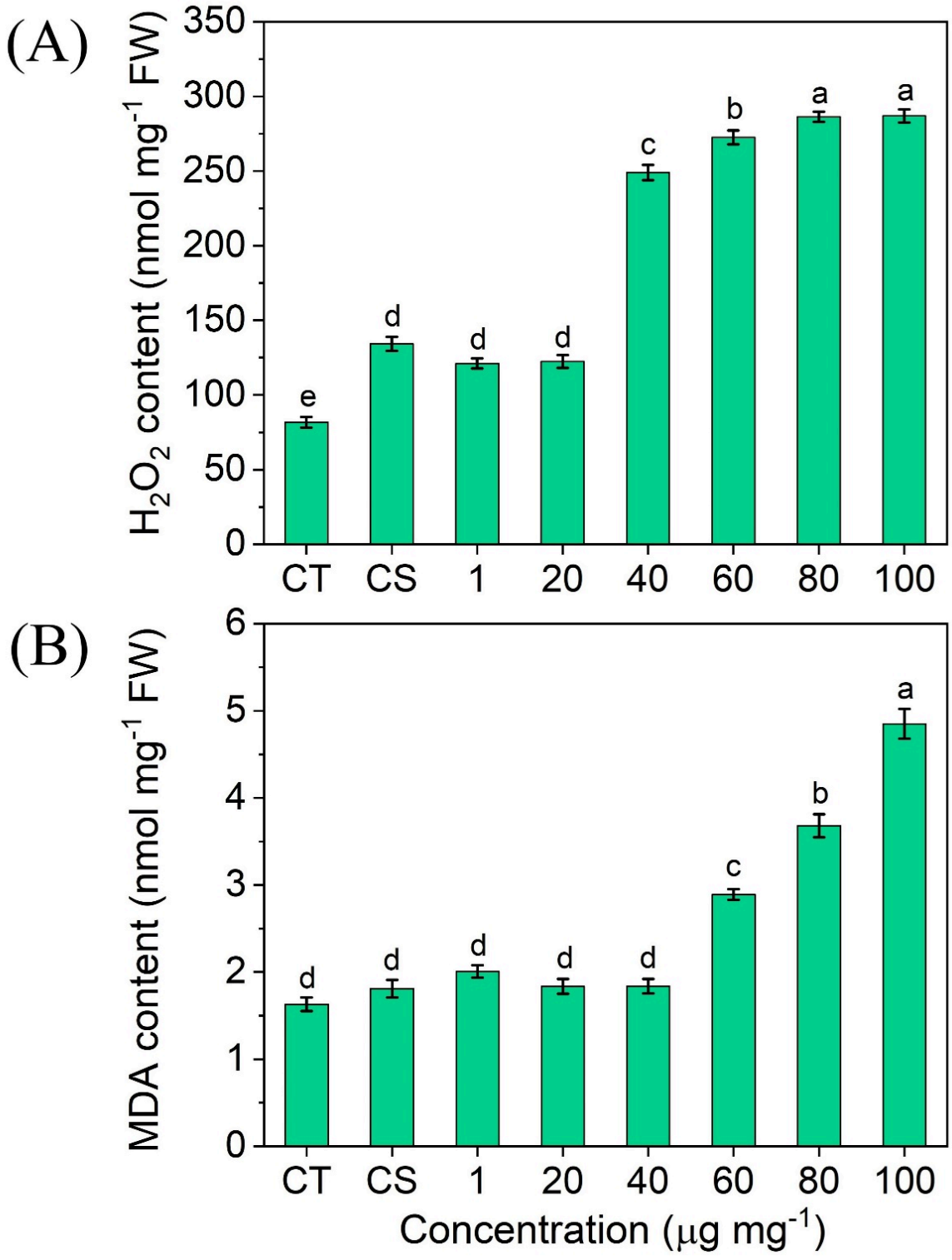

Figure 10

Effect of CS and CS:Fe_3O_4 NPs on hydrogen peroxide content (A). Malondialdehyde - MDA (B). Significant differences ($p < 0.05$) are represented by different letters between treatments. Data are represented by the mean followed by the standard deviation (±).

Supplementary Files

This is a list of supplementary files associated with this preprint. Click to download.

- floatimage1.jpeg